

Rigorous coupled-wave analysis of liquid crystal polarization gratings

JIANGHAO XIONG  AND SHIN-TSON WU* 

College of Optics and Photonics, University of Central Florida, Orlando, Florida 32816, USA

*swu@creol.ucf.edu

Abstract: Several types of liquid crystal polarization gratings (LCPGs) can be achieved depending on their molecular configurations and diffraction properties. We perform detailed numerical studies of these LCPGs based on the rigorous coupled-wave analysis (RCWA) approach. The unique properties of Raman-Nath and Bragg gratings are investigated, and how the transition between them influences the diffraction behaviors is explained. Two types of LCPGs, corresponding to the planar and the slanted director configurations, are compared in detail. The influence of gradient-pitch on the performance of reflection grating is also explored. Potential applications of these LCPGs for near-eye displays are emphasized.

© 2020 Optical Society of America under the terms of the [OSA Open Access Publishing Agreement](#)

1. Introduction

Liquid crystal polarization optical elements (LCPOEs) generally refer to the devices with spatially periodic LC director orientation, which is achieved through patterning methods like photo-alignment [1–3] or micro-rubbing [4,5]. The unique features of LCPOEs, including high diffraction efficiency, polarization sensitivity, compact form and simple fabrication process, have enabled widespread applications in beam steering [6–8], imaging [9,10], and near-eye displays [11–18]. The local region of a LCPOE, such as a LC lens [19], can be regarded as a grating. Therefore, it is important to understand the fundamental properties of liquid crystal polarization gratings (LCPGs) in order to optimize their performance. According to the LC director configuration, two types of LCPGs have been developed: transmissive polarization grating (TPG) and reflective polarization grating (RPG). A TPG is usually based on the Pancharatnam-Berry phase [1] of patterned half-wave plate where a nematic LC is employed in most cases. When the period of a TPG is large, it belongs to the Raman-Nath regime, and its response to the right-handed circularly polarized (RCP) light and left-handed circularly polarized (LCP) light is symmetric [1]. As the grating period gets smaller, the TPG gradually falls into the Bragg regime, and its response to LCP and RCP is highly asymmetric [12,20]. Detailed analyses on these different behaviors and their underlying mechanisms would help optimize the device designs. Thus, there is urgent need to develop a comprehensive numerical model for optimizing the TPG device performances.

RPGs, on the other hand, are generally built on the strong Bragg reflection, where the grating pitch is close to the optical wavelength. Therefore, a highly twisted cholesteric liquid crystal (CLC) with a small pitch is commonly used in RPGs [12,14,21,22]. Previous studies of RPGs [12,14,23,24] are based on a hypothesis that the LC directors are parallel to the substrate surface. However, it is found later this configuration can only be obtained through multiple spin-coating processes and each layer has to be thin enough (~50 nm) to prevent the LC directors from deformation [22,25]. For a bulk RPG fabricated through one-time spin-coating or cell assembly, the simulation results based on LC dynamics indicate that the LC directors follow the slanted CLC structure to keep the lowest bulk free energy [22]. To optimize the performance of these slanted PGs for various imaging and display systems like augmented reality [3,13,14], detailed analyses of their optical properties are required.

In this paper, we adopt the rigorous coupled-wave analysis (RCWA) [26–28] approach to explore these polarization gratings with high numerical accuracy and efficiency. We compare RCWA with the finite element method (FEM) to validate that RCWA is more suitable for the simulation of LCPGs, especially at large incident angles. Detailed numerical analyses are conducted for TPG, RPG, planar PG, and slanted PG. These results not only shed new light to the diffraction properties of various LCPGs, but also provides useful guidelines for optimizing the LCPG designs for different applications like imaging and near-eye displays.

2. Liquid crystal polarization gratings

All the above-mentioned LCPGs are commonly fabricated through the polarization holography using LCP and RCP to form sinusoidal linearly polarized pattern, as Fig. 1(a) depicts. These patterns are replicated onto the photo-alignment layer upon exposure. A reactive mesogen (or LC) is then placed on the photo-alignment layer to form the LCPG through spin-coating (or cell assembly).

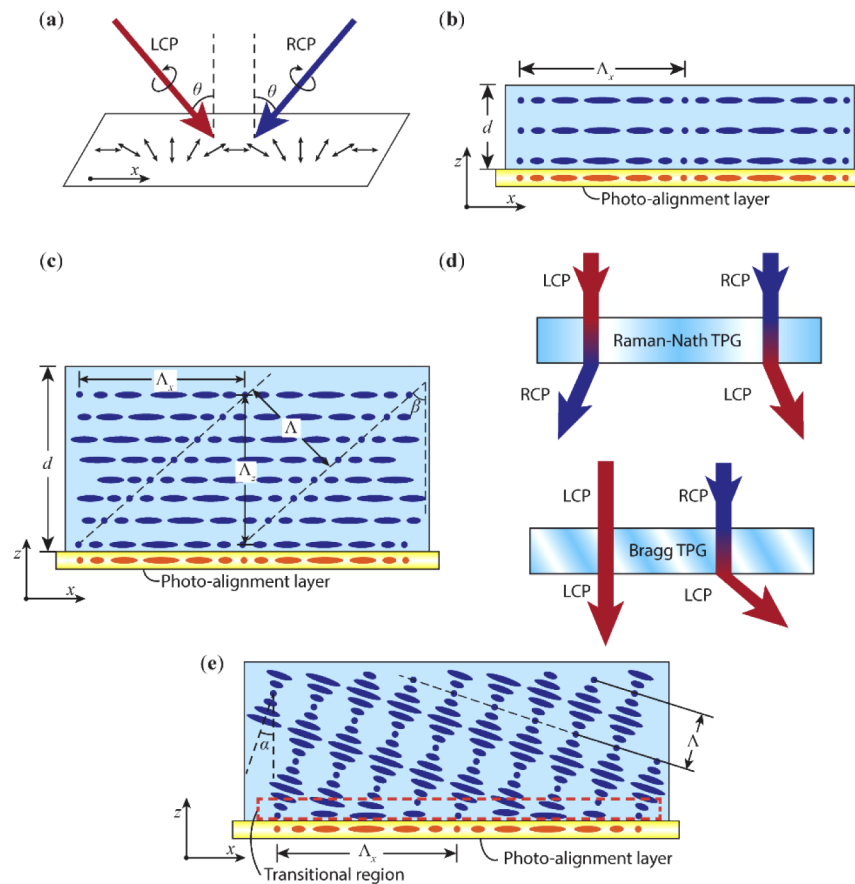


Fig. 1. Device configurations and properties of various LCPGs. (a) Sinusoidal linearly polarized pattern from the interference of LCP and RCP beams. (b) The inner LC orientation of the non-twisted transmission grating. (c) The planar-twisted structure with all LC directors parallel to the substrate and following the bottom pattern. (d) Diffraction properties of Raman-Nath and Bragg gratings. (e) Slanted configuration where the helical structure is slanted to match the bottom pattern and minimize the volume free energy.

If a nematic LC is used, the bulk LC directors will follow the bottom pattern to form TPG, as shown in Fig. 1(b). The thickness of the TPG is controlled to satisfy the half-wave retardation. Thus, the incident CP light, after passing through the TPG, will accumulate a linear phase retardation, which corresponds to the first-order diffraction. This can be explained by the following equation:

$$J_{HWP} \begin{bmatrix} 1 \\ \pm i \end{bmatrix} = \begin{bmatrix} \cos(k_0 \sin \theta \cdot x) \sin(k_0 \sin \theta \cdot x) \\ \sin(k_0 \sin \theta \cdot x) - \cos(k_0 \sin \theta \cdot x) \end{bmatrix} \begin{bmatrix} 1 \\ \pm i \end{bmatrix} = \begin{bmatrix} 1 \\ \mp i \end{bmatrix} e^{\pm i k_0 \sin \theta \cdot x} \quad (1)$$

where J_{HWP} is the Jones matrix of the rotated half-wave plate, θ is the incident angle of the recording light in Fig. 1(a) and k_0 is the wavenumber. This type of phase accumulation through the difference in the local spatial rotation is called geometric phase or Pancharatnam-Berry (PB) phase. From Eq. (1), the accumulated PB phase for the LCP light is opposite to that of the RCP light, indicating they have opposite diffraction directions. The handedness of the incident CP light is also flipped after passing the TPG. This type of TPG has the simplest configuration, but its spectral and angular bandwidths are limited because this simple half-wave plate has serious angular and spectral dispersions. To improve the performance, a twist in the z direction can be introduced by adding some chiral dopants to the nematic LC, as Fig. 1(c) shows. The angle between the Bragg surface and substrate normal is defined as β , which signifies the degree of tilting. If the chiral concentration is not too high, the bulk can maintain planar structure and follow the bottom pattern accordingly. This twisted-planar structure is usually used in the multilayer form with a separate thickness and twist angle for each layer. With such a design freedom, a broadband LCPG can be fabricated [16,29–31].

Another usage of twisted-planar structure occurs in the Bragg TPG. To classify the PGs, we can use the so-called Q factor [32] which is defined as $Q=2\pi\lambda d/(\bar{n}\Lambda)^2$, where λ is the wavelength, d is the grating thickness, \bar{n} is the average refractive index, and Λ is the grating period. When $Q < 1$ or $Q \gg 1$, the grating is classified as Raman-Nath or Bragg grating, respectively. For a Raman-Nath TPG, the incident LCP and RCP lights will have opposite but symmetric diffraction angles. As shown in Fig. 1(d), the incident LCP light is deflected toward an opposite direction to the incident RCP light, with both incident lights flipping the handedness after the Raman-Nath TPG. As the grating period gets smaller, which corresponds to a larger diffraction angle, the grating gradually transits to Bragg regime. At this point, to keep a high efficiency at normal incidence, some chiral dopants must be added to the LC host to form the twisted PG. The PG, while still manifests high polarization sensitivity, responds quite differently to different CP lights, as Fig. 1(d) depicts. The Bragg TPG transmits the LCP and preserves its polarization state but diffracts the RCP while flipping its handedness. In Section 3, we will explain the cause of this difference.

When the chiral concentration is further increased, the grating period in z direction Λ_z will become smaller than that in x direction Λ_x . At this point, the TPG transits to RPG. However, as mentioned earlier, the high chiral concentration causes the LC alignment problem and to maintain twisted-planar structure requires an even thinner single layer during the multiple spin-coating process. A more practical way to fabricate RPG is to directly form the bulk structure with a single spin-coating [22] or cell assembly [21,22], which forms the slanted structure sketched in Fig. 1(e). The angle between the helical axis and substrate normal is defined as α . Note that $\beta=90^\circ-\alpha$ [Fig. 1(c)] in terms of Bragg surface position. This slanted RPG has a transitional region in the bottom where the LC directors change from planar to slanted helical structure. The thickness of this region is usually very thin (~ 50 nm) so its total contribution to the free energy is negligible. In fact, this thickness is somewhat related to the single layer thickness from each spin-coating process during the planar RPG fabrication. In principle, the slanted structure can also be adopted to fabricate TPGs. For example, by adjusting the chiral concentration and bottom

alignment period, the slant angle can be large enough to establish transmissive Bragg diffractions [22]. In Section 3, we will investigate the properties of slanted PGs (both TPG and RPG) and compare with those of planar PGs.

3. Numerical analysis of LCPG

3.1. RCWA for anisotropic gratings

RCWA is an effective method in computational electromagnetics to solve the diffraction problems in periodic structures. It denotes the electromagnetic fields in the Fourier expansion form and uses the matrix representation to solve the Maxwell equations. In the early stage, it was used to study the surface relief gratings with binary refractive index distribution [26,27]. The approximation of binary grating requires many Fourier orders to achieve high accuracy. However, in the case of LCPGs, the distribution of the dielectric tensor is smooth and oftentimes has only one or two prominent orders. Therefore, it only requires few computational orders to produce adequate accuracy. To implement RCWA to analyze our anisotropic LCPGs, we adopt the most general form of dielectric tensor. Another feature of our RCWA formulation involves the treatment of grating period in z direction. One way to tackle the varying structure in z direction is to divide the grating into multiple layers. Transmission or scattering matrix method can be used to connect the wave coefficients of contacting layers. This, however, can significantly slow down the computation speed due to increased layer number. Here, by incorporating the z -direction period into RCWA formula, we avoid this issue and treat the grating as a single layer, which leads to fast computation speed. Details of the RCWA formulation, including the definitions of plane-of-incidence, polarization states and local coordinates, can be found in the Supplemental Document.

First, we compare the RCWA and FEM methods using RPG as an example. The configuration in RCWA simulation consists of the PG sandwiched between glass substrates with infinite thickness. For the RCWA method, we find that when the order number M is greater than 4, the yielded result stays almost the same. During the computation, we set $M=6$. In FEM simulation, we use COMSOL Multiphysics for the implementation. The PG is placed between glass substrates whose thickness is 500 nm. The thickness of glass is not critical to the simulation. Perfect matching layers (PMLs) with 2- μm thickness are placed in contact with the glass. The input and output ports are set at the PML-glass interfaces. The wavelength is set at 500 nm, the grating pitch is $\Lambda=388$ nm, the grating slant angle $\alpha=25^\circ$, and the refractive indices are $n_e=1.655$, $n_o=1.550$, and $n_{\text{glass}}=1.580$. The incident angle in the glass is varied from -80° to 80° . Results are shown in Fig. 2(a). In the small angle region ($<50^\circ$), both FEM and RCWA produce similar results. However, the difference becomes more obvious as the incident angle exceeds 50° . To understand the reason, we plot the sum of efficiencies of all diffraction orders (right axis). The inherent nature of RCWA promises the efficiency sum being always equal to 1. But for FEM, due to the poor absorption ability of the PML layer at large incident angles [33], the summed efficiency is greater than 1, which leads to inaccurate results.

In terms of computational speed, each calculation cycle takes about 2.4 ms for RCWA and 3.3 s for FEM, i.e., RCWA is about 1400x faster. Such a fast speed of RCWA allows us to study the PG properties with multiple variables to have a more comprehensive understanding.

3.2. Properties of TPG

In order to understand the transition from Raman-Nath TPG to Bragg TPG, we first study the Raman-Nath TPG with the same material refractive indices as listed above. The thickness is set at 1.67 μm to satisfy the half-wave condition and the grating period depicted in Fig. 1(b) is 4 μm , which leads to $Q=0.13$. The incident light is LCP and the diffraction efficiencies for the 1st transmission orders $T(+1)$ and $T(-1)$ are plotted in Figs. 2(b) and 2(c). The 2D plot in

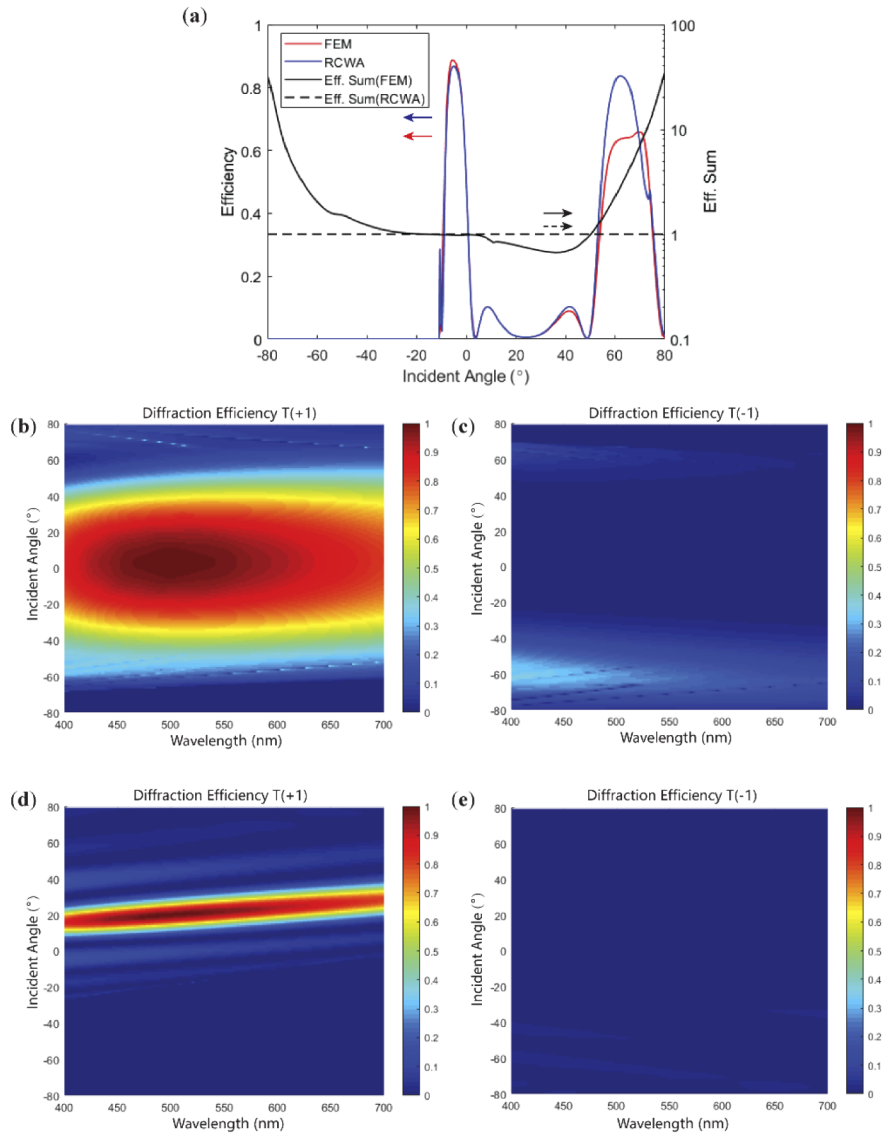


Fig. 2. (a) Angular response calculated by RCWA (red line, left axis) and FEM methods (blue line, left axis) and the summed efficiency for RCWA (black dashed lines, right axis) and FEM (black solid line, right axis). Plot of relation between wavelength-incident angle and efficiency of the Raman-Nath TPG for the (b) T(+1) order and (c) T(-1) orders with LCP incident light. Simulation results of the non-twist Bragg TPG for the (d) T(+1) order and (e) T(-1) orders with LCP incident light.

Fig. 2(b) has a clear wide high-efficiency band, where the wavelength and incident angle well satisfy the half-wave condition. For the T(-1) order in Fig. 2(c), the efficiency is generally low, indicating that for the LCP light only T(+1) diffraction order is prominent. For the incident RCP light, due to the symmetric grating structure, the diffraction efficiency is symmetric to the zero-incident-angle line, but the cases for T(-1) and T(+1) are switched, with T(-1) manifesting a high efficiency. Because the efficiency at normal incidence for both RCP and LCP is high, the diffractions are symmetric as plotted in Fig. 1(d).

As the grating pitch gets smaller, the TPG falls into Bragg regime. Here we set the grating pitch as 500 nm, while keeping other parameters the same, which yields $Q = 8.6$. The calculated $T(+1)$ and $T(-1)$ efficiencies for the incident LCP light are plotted in Figs. 2(d) and 2(e). Compared to Fig. 2(b), the high-efficiency band in Fig. 2(d) is clearly narrower, also deviating from the central zero-incident-angle position. This means the normal incident light no longer has a high efficiency, which can be understood by the fact that the light propagating in the grating already has a large angle and therefore experiences additional refractive index change in x-direction. The diffraction efficiency for the $T(-1)$ order still remains negligible. To achieve high efficiency at normal incidence, the twisted-planar structure shown in Fig. 1(c) can be considered. Here, we use the configuration with $\beta=20^\circ$ in Fig. 1(c), which somewhat coincides with the approximate 20° deviation from the center in Fig. 2(d). The $T(+1)$ diffraction efficiency for LCP light is plotted in Fig. 3(a). The band now shifts toward the center, having a high efficiency at normal incidence in the wavelength range from 450 nm to 550 nm. This kind of band shifting also occurs in the $T(-1)$ diffraction for RCP light. As plotted in Fig. 3(b), the band shifts further to around 40° , which is twice the original deviation from the center. This large band separation for LCP and RCP leads to the phenomena shown in Fig. 1(d). For LCP light, the normal incidence falls right into the band, which yields high diffraction efficiency and flips the light handedness due to Eq. (1). But for RCP, the normal incidence falls out of the band in Fig. 3(b), the diffraction efficiency is low, and the grating overall exerts no influence to the RCP light. This well explains the origin of the asymmetry in Bragg TPG in Fig. 1(d).

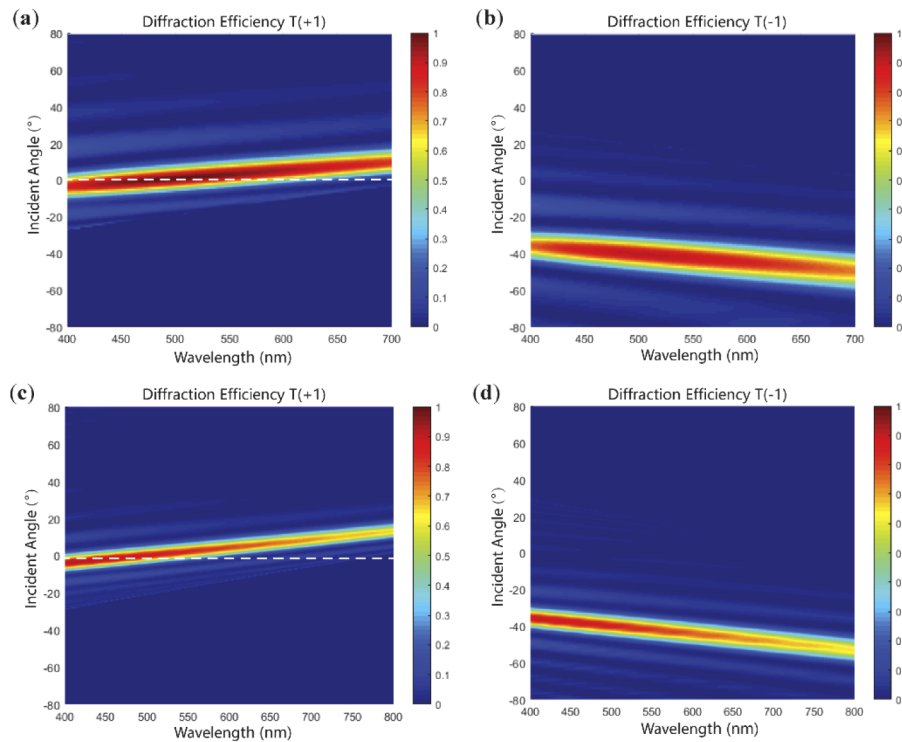


Fig. 3. Wavelength-incidence-efficiency plot of a twisted Bragg TPG for (a) $T(+1)$ order with LCP incident light and (b) $T(-1)$ order with RCP incident light. Wavelength-incidence-efficiency plot of slanted Bragg TPG for (c) $T(+1)$ and (d) $T(-1)$ order with TE incident light.

Aside from the twisted-planar structure (planar PG) which requires multiple spin-coating to maintain the planar structure, slanted PG can also function as TPGs. Because the main difference between TPG and RPG is the Bragg surface slant angle, by controlling the chiral concentration and bottom alignment period we can arbitrarily tune the slant angle of slanted PG to make it transmissive [22]. Therefore, we also simulate the diffraction efficiency of the slanted TPG, with completely the same grating pitches as the planar TPG, but different inner LC molecular orientation and the grating thickness. The grating thickness is adjusted to be $2.5\ \mu\text{m}$ to have a relatively large efficiency in the visible region. This is because when the LC molecules are tilted, the effective phase retardation decreases, so a larger thickness is required to maintain the same efficiency.

During simulation, we find an interesting feature of this slanted TPG that it only responds to linearly polarized TE light. For TM light, the diffraction efficiency is so small for all the orders that we do not include these data. The T(+1) and T(-1) diffraction efficiencies under TE polarization are plotted in Figs. 3(c) and 3(d). The efficiency bands are narrower compared to the planar TPG. The maximum efficiency is also slightly decreased to around 0.9, but the positions of the efficiency band are similar to those of planar TPG because of the same grating configuration. It should be noted that the similarity between Figs. 3(a) and 3(b) and Figs. 3(c) and 3(d) should not be interpreted as the similarity of the grating properties. As previously illustrated, Figs. 3(a) and 3(b) are under opposite incident polarization states, which means for one CP state there exists one and only one high efficiency band in either T(-1) or T(+1) order. But for slanted TPG, the high-efficiency bands only occur in linear TE polarization.

For a slanted TPG whose property only responding to TE light is because the grating at this point resembles the lying helix (LH) structure [34,35] where the CLC helix are parallel to the substrate. For the LH structure, TM light has its electric field parallel to the helix, seeing only short axis of CLC (n_o) and therefore experiencing no index modulation. TE light, on the other hand, sees both long and short axes and can be diffracted by the LH structure. Still, the helix of slanted TPG is not completely parallel to the substrate so TM light can still have a weak response (~ 0.1). This response decreases as the helix becomes more parallel to the substrate.

3.3. Properties of RPG

Because for RPG, the slanted structure is easier to fabricate and therefore more widely adopted. We first study the slanted-RPG, with grating pitch $\Lambda=190\ \text{nm}$, thickness $d=2.5\ \mu\text{m}$ and slant angle $\alpha=20^\circ$ depicted in Fig. 1(c). The material refractive indices are the same as above. The simulated results are plotted in Figs. 4(a)–4(c). The efficiency band in Fig. 4(a) is much different from the previous TPG case and has a parabolic shape symmetric around the 20° incident angle, which coincides with the slant angle. This phenomenon can be understood with the example of CLC reflection. When the Bragg surface is parallel to the substrate, the whole structure is symmetric, and the efficiency band would have the same shape as the one in Fig. 4(a) but the symmetry is around the zero incidence line. A larger incidence would cause the blue-shift of the band, while decreasing the bandwidth. But when the CLC structure is slanted, the band also shifts accordingly, moving the symmetry line to the one corresponding to the slant angle. This causes different angular band-shifting behaviors. As plotted in Fig. 4(b), the spectral band at zero incidence has a peak around 550 nm. As the incident angle increases to 20° , the peak red-shifts to 600 nm. When the incident angle further increases to 40° , the peak then experiences a blue-shift and is moved to around 550 nm again, but the bandwidth is slightly wider than that at normal incidence.

The angular responses have an even larger variation. Because the band shape is parabolic, it is possible to have different angular bands at the same wavelength. As shown in Fig. 4(c), at $\lambda = 550\ \text{nm}$, the left band is nearly symmetric to the zero incidence, but the second band peaks at around 40° . These two bands are symmetric to 20° incident angle due to the band symmetry

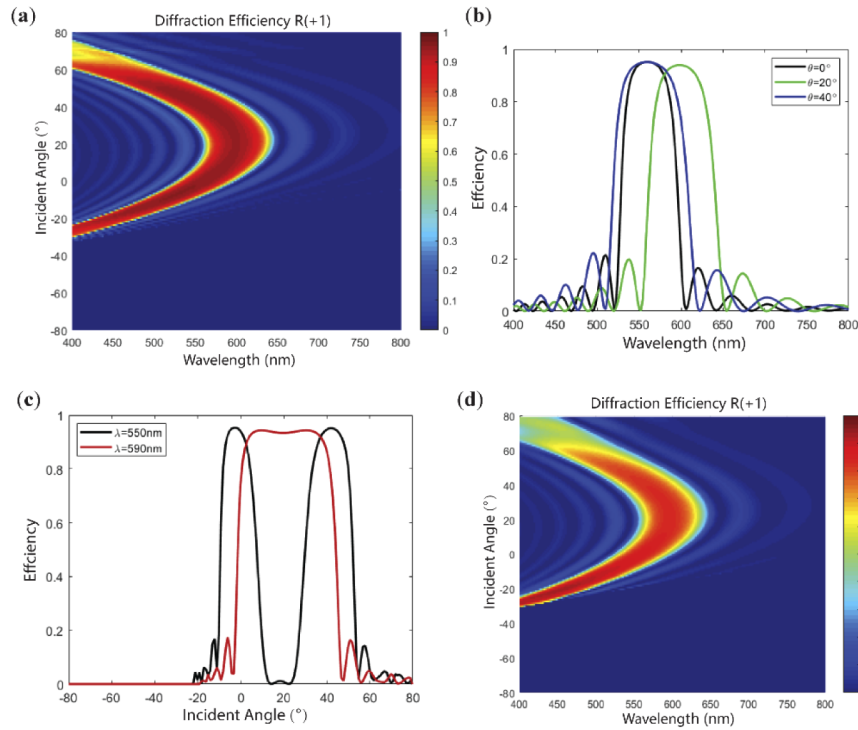


Fig. 4. (a) Wavelength-incidence-efficiency plot of the slanted-RPG. (b) Wavelength-efficiency plot of the slanted RPG with different incident angles. (c) Incidence-efficiency plot of the slanted RPG with different wavelengths. (d) Wavelength-incidence-efficiency plot of the planar-RPG.

property. As the wavelength gets longer, the two bands move closer to each other and finally reach a state when two bands are merged into one. As plotted in Fig. 4(d), under $\lambda = 590\text{ nm}$, the merged band has a peak at about 20° and the bandwidth is about 42° .

For the planar RPG, Fig. 4(d) shows the simulated results. The band shape is generally the same as that of slanted RPG because all the grating parameters are kept the same. But the highest efficiency is around 0.8, which is lower than the value of 0.95 for the slanted RPG. This is because for the reflection mode, the perfect CLC helical structure in the slanted RPG can have the strongest Bragg reflection. However, it should be mentioned that the efficiency for both planar- and slanted-RPGs can be further improved to be close to 1 by increasing the grating thickness. The width of the band, however, is largely determined by the LC birefringence. In the simulation, we use $\Delta n=0.15$. There are many LC materials with larger birefringence, which helps to significantly increase both angular and spectral bandwidths.

3.4. Gradient-pitch RPG

Another way to widen the spectral bandwidth is to introduce gradient-pitch (GP) structure using UV dye and the diffusion behavior of LC monomers [36–38]. Namely, when an absorptive dye is doped to the LC material, the UV light intensity would decrease exponentially along the incident direction. The region with a higher intensity would consume the monomers at a higher rate, forcing the monomers to diffuse to that region, which in turn causing the gradient chiral concentration. As depicted in Fig. 5(a), the bottom pitch Λ_x is fixed along the x direction, but the gradient CLC pitch in z direction causes the slant angle changing from α_1 to α_2 . The simulation

of the gradient-pitch RPG involves the multi-layer RCWA with improved transmission matrix method [39]. Here, we keep Λ_x the same as the previous cases and the slant angle changes from $\alpha_1 = 17^\circ$ to $\alpha_2 = 23^\circ$. The grating thickness is set at $5 \mu\text{m}$. In z direction, we slice the grating into 20 layers, above which the simulation results stay unchanged.

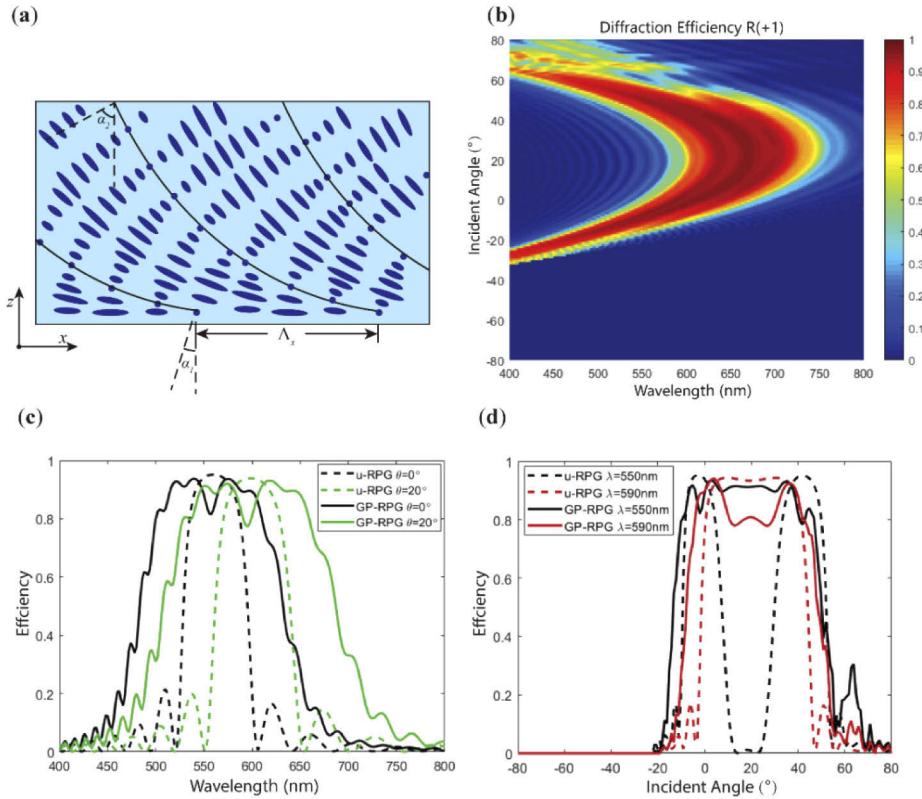


Fig. 5. (a) Sketch of the gradient-pitch (GP) slanted RPG, with fixed grating pitch in x direction and variable pitch in z direction. (b) Wavelength-incidence-efficiency plot of the GP RPG. (c) Wavelength-efficiency plot of the GP RPG with different incident angles. (d) Incidence-efficiency plot of the GP RPG with different wavelengths.

The simulation results are plotted in Figs. 5(b) and 5(c). The efficiency band in Fig. 5(b) still maintains the parabolic shape, but the band is stretched along the wavelength direction as compared to the one in Fig. 4(a). Also, some nonuniformity is observed in the high-efficiency region, which results from the interference of various bands corresponding to different slant angles. Increasing the grating thickness would ultimately eliminate this efficiency non-uniformity. To further analyze the difference, we plot the spectral and angular responses in comparison with the uniform RPG (u-RPG) cases in Figs. 5(c) and 5(d). From Fig. 5(c), the spectral bandwidth at zero incidence increases from 70 nm to 160 nm. For the 20° incidence, the bandwidth increases from 80 nm to 190 nm. From Fig. 5(d), the angular band at $\lambda=550 \text{ nm}$ is changed to single-peak band. The angular bandwidth is increased to around 60° . The band at $\lambda=590 \text{ nm}$ has a lower valley in the center due to the non-uniform efficiency. The angular bandwidth is also increased to 55° .

3.5. Tolerance analysis

To provide useful guidance and insights to practical fabrications and designs, we perform tolerance analysis on how the variations of grating parameters influence the diffraction efficiency. To be specific, the grating thickness, pitch and slant angle are varied for planar-TPG, slanted-TPG and slanted-RPG to observe the change in diffraction efficiency. For both TPGs, the input light is $\lambda = 520$ nm and at normal incidence. The central thickness is $1.67 \mu\text{m}$ for the planar-TPG and $3 \mu\text{m}$ for the slanted-TPG. The central grating pitch is 500 nm and central slant angle is $\alpha = 20^\circ$. The incident polarization is LCP for planar-TPG and TE for slanted-TPG. Results of tolerance analysis for TPGs are plotted in Figs. 6(a), 6(b), and 6(c). For the thickness variation shown in Fig. 6(a), planar-TPG shows a higher sensitivity than slanted-TPG. But the maximum efficiency of slanted-TPG is generally below 0.9 . This is because the polarization state corresponding to the highest efficiency is not a pure TE state. For planar-TPG, the highest efficiency is near 100% which corresponds to a perfect half-wave retardation. The dependencies of diffraction efficiency on pitch and slant angle variation for planar-TPG show a slightly lower sensitivity than for slanted-TPG, as shown in Fig. 6(b) and Fig. 6(c).

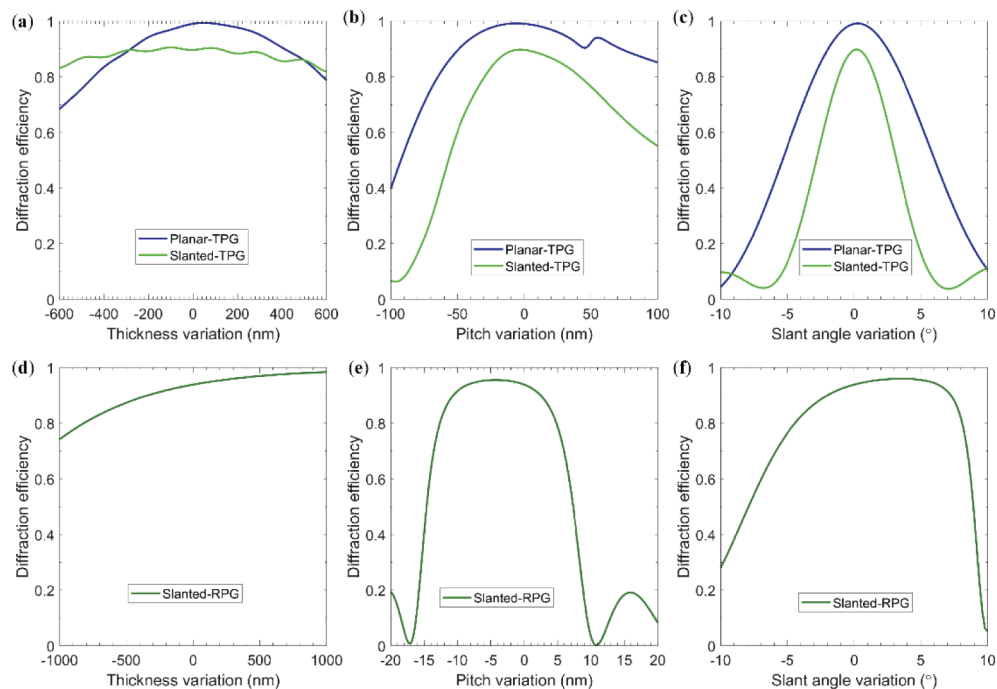


Fig. 6. Results of tolerance analysis. The change of diffraction efficiency regarding the variation of (a) grating thickness, (b) grating pitch and (c) slant angle for planar-TPG and slanted-TPG. The change of diffraction efficiency regarding the variation of (d) grating thickness, (e) grating pitch and (f) slant angle for slanted-RPG.

For a slanted-RPG, the results are shown in Figs. 6(d) to 6(f). The diffraction efficiency variation on thickness is not too sensitive and has a monotonic increasing trend, as plotted in Fig. 6(d). This is typical for reflective gratings. The sensitivity of diffraction efficiency on pitch shown in Fig. 6(e) is higher than that in TPGs. One reason is the small pitch of RPG, which results in a larger relative pitch variation than in TPGs. Another reason is that the center of Bragg band in RPGs is highly dependent on the pitch. The variation of pitch therefore moves the Bragg band dramatically. In contrast, the Bragg band center in TPGs is more dependent on the grating

thickness and is less sensitive to the pitch variation. Finally, regarding the variation of slant angle, the diffraction efficiency plotted in Fig. 6(f) shows a lower sensitivity than that of TPGs.

4. Conclusion

Based on RCWA, we develop an accurate and efficient computational model for simulating the properties of LCPGs. The diffraction properties of planar TPGs in Raman-Nath and Bragg regimes are studied in detail and the origin of the asymmetric diffraction properties in Bragg TPG is explained. The diffraction behavior of slanted TPG is also investigated and compared to that of planar TPG. For RPGs, the diffraction properties are thoroughly analyzed and discussed, along with how the gradient pitch impacts the diffraction properties.

Funding

GoerTek Electronics.

Acknowledgment

The UCF group is indebted to Dr. Kun Li for useful discussion.

Disclosures

The authors declare no conflicts of interest.

See [Supplement 1](#) for supporting content.

References

1. T. Zhan, Y.-H. Lee, G. Tan, J. Xiong, K. Yin, F. Gou, J. Zou, N. Zhang, D. Zhao, J. Yang, S. Liu, and S.-T. Wu, "Pancharatnam-Berry optical elements for head-up and near-eye displays [Invited]," *J. Opt. Soc. Am. B* **36**(5), D52–D65 (2019).
2. L. De Sio, D. E. Roberts, Z. Liao, S. Nersisyan, O. Uskova, L. Wickboldt, N. Tabiryan, D. M. Steeves, and B. R. Kimball, "Digital polarization holography advancing geometrical phase optics," *Opt. Express* **24**(16), 18297–18306 (2016).
3. Y.-H. Lee, G. Tan, T. Zhan, Y. Weng, G. Liu, F. Gou, F. Peng, N. V. Tabiryan, S. Gauza, and S.-T. Wu, "Recent progress in Pancharatnam–Berry phase optical elements and the applications for virtual/augmented realities," *Opt. Data Process. Storage* **3**(1), 79–88 (2017).
4. M. Honma and T. Nose, "Highly efficient twisted nematic liquid crystal polarization gratings achieved by microrubbing," *Appl. Phys. Lett.* **101**(4), 041107 (2012).
5. M. Honma and T. Nose, "Twisted nematic liquid crystal polarization grating with the handedness conservation of a circularly polarized state," *Opt. Express* **20**(16), 18449–18458 (2012).
6. C. Oh, J. Kim, J. Muth, S. Serati, and M. J. Escuti, "High-Throughput Continuous Beam Steering Using Rotating Polarization Gratings," *IEEE Photonics Technol. Lett.* **22**(4), 200–202 (2010).
7. J. Kim, C. Oh, S. Serati, and M. J. Escuti, "Wide-angle, nonmechanical beam steering with high throughput utilizing polarization gratings," *Appl. Opt.* **50**(17), 2636–2639 (2011).
8. H. Chen, Y. Weng, D. Xu, N. V. Tabiryan, and S.-T. Wu, "Beam steering for virtual/augmented reality displays with a cycloidal diffractive waveplate," *Opt. Express* **24**(7), 7287–7298 (2016).
9. H. Ono, T. Wada, and N. Kawatsuki, "Polarization Imaging Screen Using Vector Gratings Fabricated by Photocrosslinkable Polymer Liquid Crystals," *Jpn. J. Appl. Phys.* **51**, 030202 (2012).
10. M. W. Kudenov, M. J. Escuti, E. L. Dereniak, and K. Oka, "White-light channeled imaging polarimeter using broadband polarization gratings," *Appl. Opt.* **50**(15), 2283–2293 (2011).
11. C. Yoo, J. Xiong, S. Moon, D. Yoo, C.-K. Lee, S.-T. Wu, and B. Lee, "Foveated display system based on a doublet geometric phase lens," *Opt. Express* **28**(16), 23690–23702 (2020).
12. Y. Weng, D. Xu, Y. Zhang, X. Li, and S.-T. Wu, "Polarization volume grating with high efficiency and large diffraction angle," *Opt. Express* **24**(16), 17746–17759 (2016).
13. Y. Weng, Y. Zhang, J. Cui, A. Liu, Z. Shen, X. Li, and B. Wang, "Liquid-crystal-based polarization volume grating applied for full-color waveguide displays," *Opt. Lett.* **43**(23), 5773–5776 (2018).
14. Y.-H. Lee, K. Yin, and S.-T. Wu, "Reflective polarization volume gratings for high efficiency waveguide-coupling augmented reality displays," *Opt. Express* **25**(22), 27008–27014 (2017).

15. J. Xiong, G. Tan, T. Zhan, and S.-T. Wu, "Wide-view augmented reality display with diffractive cholesteric liquid crystal lens array," *J. Soc. Inf. Disp.* **28**, 450–456 (2020).
16. T. Zhan, J. Zou, J. Xiong, X. Liu, H. Chen, J. Yang, S. Liu, Y. Dong, and S.-T. Wu, "Practical Chromatic Aberration Correction in Virtual Reality Displays Enabled by Cost-Effective Ultra-Broadband Liquid Crystal Polymer Lenses," *Adv. Opt. Mater.* **8**, 1901360 (2020).
17. T. Zhan, J. Xiong, G. Tan, Y.-H. Lee, J. Yang, S. Liu, and S.-T. Wu, "Improving near-eye display resolution by polarization multiplexing," *Opt. Express* **27**(11), 15327–15334 (2019).
18. T. Zhan, Y.-H. Lee, and S.-T. Wu, "High-resolution additive light field near-eye display by switchable Pancharatnam-Berry phase lenses," *Opt. Express* **26**(4), 4863–4872 (2018).
19. K. Gao, H.-H. Cheng, A. K. Bhowmik, and P. J. Bos, "Thin-film Pancharatnam lens with low f-number and high quality," *Opt. Express* **23**(20), 26086–26094 (2015).
20. K. Yin, T. Zhan, J. Xiong, Z. He, and S.-T. Wu, "Polarization Volume Gratings for Near-Eye Displays and Novel Photonic Devices," *Crystals* **10**(7), 561 (2020).
21. R. Chen, Y.-H. Lee, T. Zhan, K. Yin, Z. An, and S.-T. Wu, "Multistimuli-Responsive Self-Organized Liquid Crystal Bragg Gratings," *Adv. Opt. Mater.* **7**, 1900101 (2019).
22. J. Xiong, R. Chen, and S.-T. Wu, "Device simulation of liquid crystal polarization gratings," *Opt. Express* **27**(13), 18102–18112 (2019).
23. X. Xiang and M. J. Escuti, "Numerical analysis of Bragg polarization gratings," *J. Opt. Soc. Am. B* **36**(5), D1–D8 (2019).
24. X. Xiang, J. Kim, and M. J. Escuti, "Bragg polarization gratings for wide angular bandwidth and high efficiency at steep deflection angles," *Sci. Rep.* **8**(1), 7202 (2018).
25. Y.-H. Lee, Z. He, and S.-T. Wu, "Optical properties of reflective liquid crystal polarization volume gratings," *J. Opt. Soc. Am. B* **36**(5), D9–D12 (2019).
26. M. G. Moharam, E. B. Grann, D. A. Pommet, and T. K. Gaylord, "Formulation for stable and efficient implementation of the rigorous coupled-wave analysis of binary gratings," *J. Opt. Soc. Am. A* **12**(5), 1068–1076 (1995).
27. M. G. Moharam and T. K. Gaylord, "Rigorous coupled-wave analysis of planar-grating diffraction," *J. Opt. Soc. Am.* **71**(7), 811–818 (1981).
28. E. N. Glytsis and T. K. Gaylord, "Three-dimensional (vector) rigorous coupled-wave analysis of anisotropic grating diffraction," *J. Opt. Soc. Am. A* **7**(8), 1399–1420 (1990).
29. K. Gao, C. McGinty, H. Payson, S. Berry, J. Vornehm, V. Finnmeyer, B. Roberts, and P. Bos, "High-efficiency large-angle Pancharatnam phase deflector based on dual-twist design," *Opt. Express* **25**(6), 6283–6293 (2017).
30. J. Zou, T. Zhan, J. Xiong, and S.-T. Wu, "Broadband wide-view Pancharatnam-Berry phase deflector," *Opt. Express* **28**(4), 4921–4927 (2020).
31. C. Oh and M. J. Escuti, "Achromatic diffraction from polarization gratings with high efficiency," *Opt. Lett.* **33**(20), 2287–2289 (2008).
32. M. G. Moharam and L. Young, "Criterion for Bragg and Raman-Nath diffraction regimes," *Appl. Opt.* **17**(11), 1757–1759 (1978).
33. S. G. Garcia, I. V. Perez, R. G. Martin, and B. G. Olmedo, "Applicability of the PML absorbing boundary condition to dielectric anisotropic media," *Electron. Lett.* **32**(14), 1270–1271 (1996).
34. A. Ryabchun and A. Bobrovsky, "Cholesteric Liquid Crystal Materials for Tunable Diffractive Optics," *Adv. Opt. Mater.* **6**, 1800335 (2018).
35. Z.-G. Zheng, Y. Li, H. K. Bisoyi, L. Wang, T. J. Bunning, and Q. Li, "Three-dimensional control of the helical axis of a chiral nematic liquid crystal by light," *Nature* **531**(7594), 352–356 (2016).
36. K. Yin, H.-Y. Lin, and S.-T. Wu, "Chirped polarization volume grating with ultra-wide angular bandwidth and high efficiency for see-through near-eye displays," *Opt. Express* **27**(24), 35895–35902 (2019).
37. D. J. Broer, J. Lub, and G. N. Mol, "Wide-band reflective polarizers from cholesteric polymer networks with a pitch gradient," *Nature* **378**(6556), 467–469 (1995).
38. M. Mitov, "Cholesteric Liquid Crystals with a Broad Light Reflection Band," *Adv. Mater.* **24**(47), 6260–6276 (2012).
39. M. G. Moharam, D. A. Pommet, E. B. Grann, and T. K. Gaylord, "Stable implementation of the rigorous coupled-wave analysis for surface-relief gratings: enhanced transmittance matrix approach," *J. Opt. Soc. Am. A* **12**(5), 1077–1086 (1995).